PNAS RESEARCH ARTICLE | ENGINEERING

Lanthanide binding peptide surfactants at air–aqueous interfaces for interfacial separation of rare earth elements

Luis E. Ortuno Macias[a], Felipe Jiménez-Ángeles[b], Jason G. Marmorstein[c], Yiming Wang[d], Stephen A. Crane[d], Surabh K. T.[a], Pan Sun[e], Bikash Sapkota[e], Eshe Hummingbird[c], Woojin Jung[d], Baofu Qiao[b], Daeyeon Lee[d], Ivan J. Dmochowski[c], Robert J. Messinger[a], Mark L. Schlossman[e], Cesar de la Fuente-Nunez[d], Ravi Radhakrishnan[d], E. James Petersson[d], Monica Olvera de la Cruz[b], Wei Bu[f], Mrinal Bera[f], Binhua Lin[f], Raymond S. Tu[a], Kathleen J. Stebe[d,1], and Charles Maldarelli[a,1]

Affiliations are included on p. 11.

Edited by David Weitz, Harvard University, Cambridge, MA; received June 12, 2024; accepted November 4, 2024

Rare earth elements (REEs) are critical materials to modern technologies. They are obtained by selective separation from mining feedstocks consisting of mixtures of their trivalent cation. We are developing an all-aqueous, bioinspired, interfacial separation using peptides as amphiphilic molecular extractants. Lanthanide binding tags (LBTs) are amphiphilic peptide sequences based on the EF-hand metal binding loops of calcium-binding proteins which complex selectively REEs. We study LBTs optimized for coordination to Tb^{3+} using luminescence spectroscopy, surface tensiometry, X-ray reflectivity, and X-ray fluorescence near total reflection, and find that these LBTs capture Tb^{3+} in bulk and adsorb the complex to the interface. Molecular dynamics show that the binding pocket remains intact upon adsorption. We find that, if the net negative charge on the peptide results in a negatively charged complex, excess cations are recruited to the interface by nonselective Coulombic interactions that compromise selective REE capture. If, however, the net negative charge on the peptide is -3, resulting in a neutral complex, a 1:1 surface ratio of cation to peptide is achieved. Surface adsorption of the neutral peptide complexes from an equimolar mixture of Tb^{3+} and La^{3+} demonstrates a switchable platform dictated by bulk and interfacial effects. The adsorption layer becomes enriched in the favored Tb^{3+} when the bulk peptide is saturated, but selective to La^{3+} for undersaturation due to a higher surface activity of the La^{3+} complex.

LBT | peptides | rare earth elements | separation | interfaces

The development of green, selective methods to separate rare earth elements (REEs) is critically important in modern technology. The REEs' luminescent, magnetic, and catalytic properties (1–4) make them essential to modern devices and green technologies. REEs are used in devices including smartphones, computers, LEDs, and optical displays (5–8) and are critical to low carbon and sustainable energy technologies including rechargeable batteries, wind turbines, solar panels, energy-efficient lighting, and hybrid and electric vehicles (4, 9–11). However, current separation methods have deleterious environmental impact which can be mitigated by bioinspired approaches.

The REEs, which include the metals lanthanum (La) through lutetium (Lu) in the lanthanides series, and yttrium (Y) and scandium (Sc), are primarily obtained by mining of ores or clays (12) from which REEs are liberated to form concentrated aqueous mixtures of trivalent lanthanum cations (Ln^{3+}). Selective separation of these mixtures is challenging because of the REEs' identical charge, and similarity in physicochemical properties. The lanthanides differ only weakly in size; across the lanthanide series, the ionic radius decreases from 1.16 Å (La^{3+}) to 0.977 Å (Lu^{3+}) (13) owing to poor shielding of the 4f orbitals, undergoing the so-called lanthanide contraction. The arrangement of their electrons minimizes covalent bonding, restricting the Ln^{3+} to ionic coordination as Lewis acids that complex with electronegative donors.

REEs are currently separated by methods that include liquid–liquid extraction (14), in which small molecule extractants complex and solubilize REEs in organic phases, solid phase extraction (15), in which ligands immobilized on diverse solid surfaces capture REEs from aqueous solutions and release them via pH changes, and biosorption-based strategies (16–21) which exploit pH-sensitive chelating ligands on surfaces of microorganisms to capture REE cations from aqueous solution (e.g., refs. 22–26). These methods suffer from relatively poor selectivity. Furthermore, the most commonly used

Significance

The present day "seeds of technology" are the rare earth elements (REEs), materials essential to modern electronics and clean, sustainable energy technologies. Their selective separation from mining feedstocks is critical in supplying the growing list of REE-dependent technologies, but mainstream purification methods rely on organic solvents in processes that are neither sustainable nor efficient. Lanthanide binding tags (LBTs), short peptides retaining binding loops which can be designed to selectively coordinate to a unique cation in a mixture, show promise as biomolecular REE extractants. Here, we demonstrate that LBTs are surface active; in solution LBTs complex selectively to a REE cation, and transport the complex to an air/water interface enabling an all-aqueous, green, energy-efficient, interfacial separation process.

The authors declare no competing interest.

This article is a PNAS Direct Submission.

[1] To whom correspondence may be addressed. Email: kstebe@seas.upenn.edu or cmaldarelli@ccny.cuny.edu.

This article contains supporting information online at https://www.pnas.org/lookup/suppl/doi:10.1073/pnas.2411763121/-/DCSupplemental.

method, liquid–liquid extraction, requires organic solvents and repeated separation stages with high potential for deleterious environmental impact.

Biomolecular REE separation platforms based on metalloproteins and their subdomains provide an important alternative approach. For example, calcium-binding proteins bind Ca^{2+} with high selectivity and affinity in evolutionarily conserved EF hand–binding domains (27–31). An EF hand–binding domain is a well-characterized calcium-binding structural motif which is found in many calcium-binding proteins such as calmodulin and troponin. The EF hand architecture consists of a binding loop which coordinates to the calcium cation and is flanked by two alpha helices; calcium-binding proteins typically contain more than one EF hand (32). The EF hands also bind the trivalent REEs, which have radii similar to Ca^{2+} and greater valency. In an important advance, isolated binding loop peptides derived from the EF hands, so-called lanthanide binding tags (LBTs), have been designed to bind selectively to particular REEs. For example, the LBT with sequence YIDTNNDGWYEGDELLA was developed by isolating the binding loop peptide from troponin, and optimizing its binding to Tb^{3+} in preference to other REEs with resulting nanomolar dissociation constant K_D. This LBT forms a coordinating sphere that wraps Tb^{3+}. The X-ray crystallographic structure of the complex reveals an eightfold coordination of Tb^{3+}; monodentate oxygen ligands at D1, N3, and D5; bidentate oxygen ligands at E9 and E12 and a backbone carbonyl of W7, the tryptophan residue with the indole group which sensitizes the Tb^{3+} fluorescence (33–36) (Fig. 1 *A* and *B*).

Other metalloproteins that bind Ln^{3+} have been identified; studies on Ln^{3+}-dependent methanol dehydrogenase enzymes (Ln-MDHs) in methylotrophs led to the isolation of the small (12 kDa) protein, lanmodulin (LanM) (37–39). The EF hands within intact LanM have picomolar K_D that are selective for the middle to light Ln^{3+} cations. Isolated peptides derived from these EF hands, however, have micromolar K_D (40). Approaches that use such biomolecular platforms to complex Ln^{3+} cations have two important advantages. First, they may allow greener all-aqueous REE extraction platforms. Second, the multidentate nature of the REE complexation may allow tuning of the coordinating polyhedra to bind preferentially to one or a group of REEs. In particular, Ishida et al. (41) have demonstrated how binding affinity is improved by the exclusion of water from the coordination structure, and has provided a rationale to optimize affinity to a preferred cation with a given ionic radius through changes in the binding loop sequence so that water is excluded.

The EF-hands within intact proteins have been exploited in separation schemes that present the protein on a supporting structure, expose the supported protein to REEs and the mixtures in aqueous solution, and release captured REEs by elution. For example, LanM has been covalently bound to agarose beads for use in a packed column for selective separation under flow (42). LanM has also been displayed on microbes (43) and covalently bound to the surface of magnetic nanoparticles (44).

REE-binding peptides have also been exploited in this arena. For example, genetically modified microbes with surface displays of LBTs have been used to capture Ln^{3+} from solution, and subsequently release them in an eluting stream containing a competitive cation (45–49). The peptide binding loop of the EF hand of LanM has been tethered to gold nanoparticles (50). Separation was achieved by incubation with REEs, centrifugation for nanoparticle recovery, and elution for REE release; a related study conjugated the peptide binding loop of the EF hand of calmodulin to polymer scaffold particles for cerium recovery (51). Genetic engineering has been used to express a fusion of a

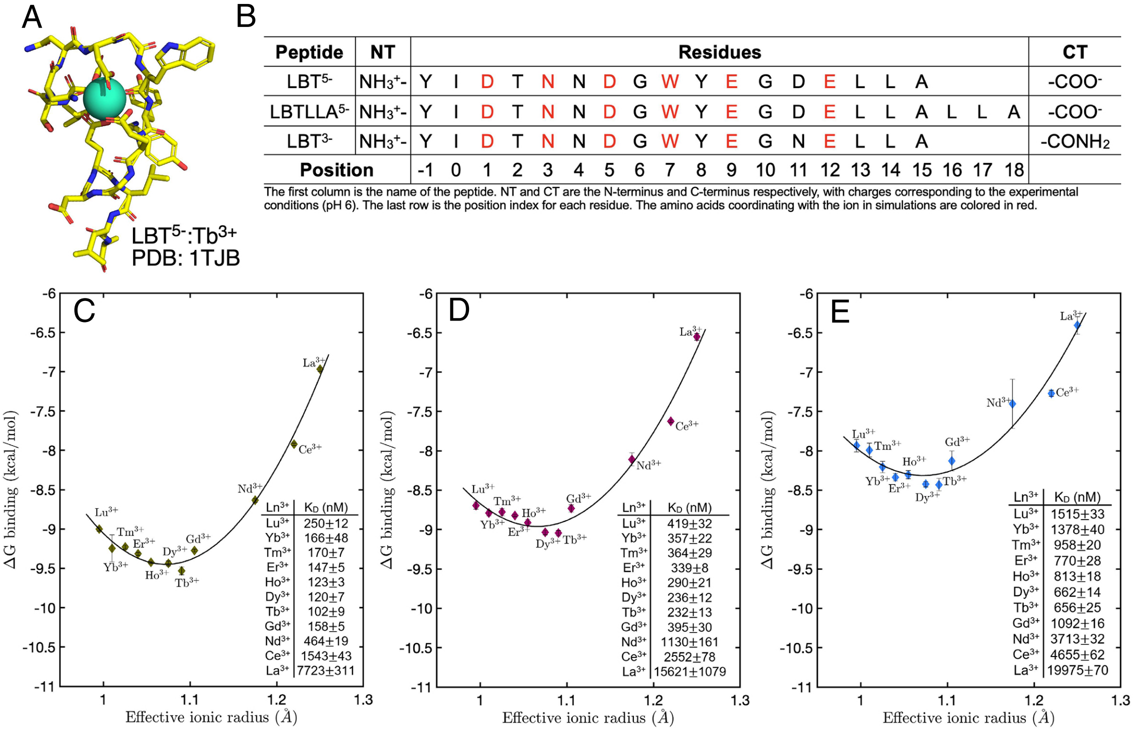

Peptide	NT	Residues																				CT
LBT^{5-}	NH_3^+-	Y	I	D	T	N	N	D	G	W	Y	E	G	D	E	L	L	A				$-COO^-$
$LBTLLA^{5-}$	NH_3^+-	Y	I	D	T	N	N	D	G	W	Y	E	G	D	E	L	L	A	L	L	A	$-COO^-$
LBT^{3-}	NH_3^+-	Y	I	D	T	N	N	D	G	W	Y	E	G	N	E	L	L	A				$-CONH_2$
Position		-1	0	1	2	3	4	5	6	7	8	9	10	11	12	13	14	15	16	17	18	

The first column is the name of the peptide. NT and CT are the N-terminus and C-terminus respectively, with charges corresponding to the experimental conditions (pH 6). The last row is the position index for each residue. The amino acids coordinating with the ion in simulations are colored in red.

Ln^{3+}	K_D (nM)
Lu^{3+}	250±12
Yb^{3+}	166±48
Tm^{3+}	170±7
Er^{3+}	147±5
Ho^{3+}	123±3
Dy^{3+}	120±7
Tb^{3+}	102±9
Gd^{3+}	158±5
Nd^{3+}	464±19
Ce^{3+}	1543±43
La^{3+}	7723±311

Ln^{3+}	K_D (nM)
Lu^{3+}	419±32
Yb^{3+}	357±22
Tm^{3+}	364±29
Er^{3+}	339±8
Ho^{3+}	290±21
Dy^{3+}	236±12
Tb^{3+}	232±13
Gd^{3+}	395±30
Nd^{3+}	1130±161
Ce^{3+}	2552±78
La^{3+}	15621±1079

Ln^{3+}	K_D (nM)
Lu^{3+}	1515±33
Yb^{3+}	1378±40
Tm^{3+}	958±20
Er^{3+}	770±28
Ho^{3+}	813±18
Dy^{3+}	662±14
Tb^{3+}	656±25
Gd^{3+}	1092±16
Nd^{3+}	3713±32
Ce^{3+}	4655±62
La^{3+}	19975±70

Fig. 1. (*A*) X-ray crystallographic structure of LBT^{5-} complexed with Tb^{3+} from Imperiali et al. (35) (PDB: 1TJB) illustrating the coordination to the cation. (*B*) Amino acid sequence of LBT^{5-}, $LBTLLA^{5-}$ and LBT^{3-} with the binding residues in red. (*C*–*E*) The free energy of association, ΔG for (*C*) LBT^{5-}, (*D*) $LBTLLA^{5-}$, and (*E*) LBT^{3-} as a function of lanthanide ionic radius with labels for the cations. The *Inset* tables provide the numerical values of K_D. The data in (*C*–*E*) was modeled to a quadratic polynomial function, represented by the lines, to enhance visualization.

thermo-responsive elastin-like polypeptide and the binding loop peptide of LanM for REE extraction; recovery was facilitated by temperature-induced phase changes followed by centrifugation (52). These studies clearly demonstrate the potential of REE-binding biomolecules for use in all-aqueous separation schemes that improve selectivity and circumvent the deleterious impact of existing approaches. In all of these studies, however, proteins or peptides are presented on tailored supports that require specialized handling. For example, the nanoparticle-based schemes require particle dispersion and recovery steps, while the hydrogel bead and microbial surface display methods must be placed in packed columns or configured for exposure to REEs feedstocks.

Ion foam flotation (IFF) is an alternative approach that exploits air–aqueous interfaces that can be formed continuously by sparging bubbles through an REEs feedstock. IFF is widely used for mineral separation and recovery. In this process, ions in aqueous solution complex to amphiphilic molecules which adsorb on rising bubbles that are collected as a foam (53–55). Importantly, IFF is an all-aqueous approach. Furthermore, IFF is amenable to continuous operation and is potentially less energy intensive as it avoids processes like centrifugation or magnetic separation. A few studies have examined using IFF for selective separation using surface active extractants (56–58), including ethylene oxide carboxylic acids, or sodium dodecyl sulfates. The surfactants' carboxylate and sulfate moieties functioned both as polar groups that provide amphiphilicity and chelating groups for REEs complexation. Not surprisingly, these studies have shown that the heavier REEs with greater Lewis acidity are favored in the extraction, a trend that is also reported in X-ray and molecular dynamics (MD) studies of the complexation of REEs to floating monolayers of insoluble phosphonic acids (59). IFF with binding loop peptides for REEs capture and separation has not yet been examined. This method would require binding loop peptides to capture REE cations in bulk, adsorb with the REE in the coordinating sphere at the interface, and to retain the captured REE cargo in the complex interfacial zone. Furthermore, to exploit the potential of the binding loops for selective REEs capture, nonselective REE–peptide interactions in the interface must be avoided.

Here, we study binding loop peptides for selective REE capture and separation at air–aqueous interfaces. We focus on the LBT peptide with sequence YIDTNNDGWYEGDELLA and its complexation to Tb^{3+}. This sequence has net charge −5; we refer to this peptide as LBT^{5-}. We note that the loop, with the carboxylate residues at the N-terminus forming the binding loop and the hydrophobic residues at the C-terminus, presents a separation of polarity that renders the peptide amphiphilic. Upon complexation at neutral pH the net charge of the LBT^{5-}:Tb^{3+} complex is −2. In addition to LBT^{5-}, we study two variants, LBTLLA^{5-}, in which the hydrophobic sequence LLA is added to the C-terminus to increase hydrophobicity, and LBT^{3-}, which forms a complex with zero net charge (Fig. 1*B*). These variants were selected to demonstrate that surface activity can be enhanced (LBTLLA^{5-}) and to show that binding loops that form neutral complexes (LBT^{3-}) can reduce nonspecific complexation. We begin by using fluorescence spectroscopy to establish that the binding affinity in bulk solution does not change considerably upon addition of the hydrophobe or the reduction in charge, and the selectivity to Tb^{3+} is retained. We next demonstrate, using surface tension measurements, that all peptide variants adsorb to the air/water interface, the addition of the −LLA increases the surface activity, and the complexed peptide is more surface active than the uncomplexed form. Using X-ray reflectivity (XR), and X-ray fluorescence near total reflection (XFNTR), we measure peptide and Tb^{3+} concentrations on the surface and demonstrate that the complexed form, upon adsorption, brings the Tb^{3+} to the air/water surface. For LBTLLA^{5-}, the ratio of cation to peptide at the surface is larger than one indicating nonspecific adsorption and for LBT^{3-}, with no net charge after complexation, the ratio of Tb^{3+} to peptide on the surface is 1. Competitive adsorption of an equimolar mixture of Tb^{3+} and La^{3+} is studied using XR and XFNTR which demonstrates a higher population of Tb^{3+} than La^{3+} when the peptide is saturated with cations, consistent with preference for Tb^{3+} in the bulk as reflected in the K_Ds. MD simulations are used to provide insight into the binding loop stability of the peptides in the bulk and at the surface, indicating that the binding loop retains the REE cation. Note importantly that the Tb^{3+} cation can be hydrolyzed to Tb(OH)$^{2+}$; however, this hydrolysis product is one percent or less of the total terbium cation at the pH (6) of the experiments; see refs. 60–62 for hydrolysis constants.

Results and Discussion

Dissociation Constants of the LBT:Ln^{3+} Complexes in Aqueous Phase. The thermodynamic bulk dissociation constants (K_D) for each of the three LBT peptide variants upon complexation with the Ln^{3+} cations are obtained by luminescence spectroscopy. This method exploits UV excitation of the tryptophan residue (position 7, Fig. 1*B*) which results in energy transfer to Tb^{3+} in the binding loop. K_Ds for Tb^{3+} are obtained by varying the cation concentration at fixed peptide concentration; K_Ds of the other lanthanides, which are not excited by tryptophan fluorescence, are obtained by competitive titration against Tb^{3+} (*Materials and Methods*).

Fig. 1 *C–E* provide the K_Ds in terms of the binding affinity or free energy of association $\Delta G = RT\ell n(K_D)$, where RT is the thermal energy. The results are plotted in terms of the lanthanide ionic radius. For LBT^{5-} (Fig. 1*C*), in agreement with the literature (35), Tb^{3+} has the highest affinity, the lighter elements having significantly weaker affinities, and the heavier elements show a smaller decrease in affinity. Fig. 1 *C–E* provide the K_Ds in terms of the binding affinity or free energy of association $\Delta G = RT\ell n(K_D)$, where RT is the thermal energy. The results are plotted in terms of the lanthanide ionic radius. For LBT^{5-} (Fig. 1*C*), in agreement with the literature (35), Tb^{3+} has the highest affinity, the lighter elements having significantly weaker affinities, and the heavier elements show a smaller decrease in affinity. The numerical values in the *Inset* are approximately twofold larger than previous reports (35). This difference can be attributed to the higher pH and amidation of the C terminus of the prior study, as detailed in *SI Appendix*.

Importantly, Fig. 1 *C–E* show clearly that the general trend in relative affinity observed for the original LBT peptide (35) is conserved in the three peptide variants. Hence the change in the C-terminus from an amide to a free acid for LBT^{5-}, the change in the C-terminus from an amide to a free acid and the addition of an −LLA to the C-terminus in the case of LBTLLA^{5-} to make the peptide more hydrophobic, or the replacement of the aspartic acid (D11) with an asparagine (N11) residue to make the complexed form uncharged (LBT^{3-}), does not alter the selectivity initially designed into the original LBT, as these variants were formed by changing noncoordinating residues in the sequence. While the relative affinities are unchanged, however, the *Inset* tables in Fig. 1 *C–E* indicate that the LLA mutation in LBTLLA^{5-} induces a consistent twofold increase in K_D, and the reduction in charge in LBT^{3-} results in an additional threefold increase when compared with the LBT^{5-} variant.

Surface Tensions of Adsorbed Layers of LBT and LBT:Tb^{3+} at the Air–Water Interface. The surface tensions of LBT solutions with and without Tb^{3+} were measured using the pendant drop technique for each variant (*Materials and Methods*). For all peptide solutions, the surface tension decreased continuously with time, indicating continuous peptide adsorption. After extended times (several thousand seconds at most), the tensions reached quasi-equilibrium values identified as a very slowly decreasing tension with time (*SI Appendix*, Fig. S1). This behavior is typical of proteins/peptides adsorbing from solution to the air/water interface; it is attributed to structural rearrangements of the adsorbed biomolecules as they gradually expose their hydrophobic groups to the air phase. These "unfolded" species do not desorb into the bulk because of their reconfiguration (63–70). Also, additional peptides in the bulk continue to adsorb, but, as the interface saturates, this adsorption is small, and generates only weak reductions in tension, contributing to the observed quasi-equilibrium behavior. The quasi-equilibrium tensions were measured for each of the LBT variants without Tb^{3+} at three concentrations (25, 50, and 100 μM), Fig. 2. The tension of the clean interface (72.8 mN/m) is recorded for a drop with only buffer and NaCl. For each variant, increasing the concentration results in a decrease in the quasi-equilibrium tension, indicating that adsorption increases with bulk concentration. For the uncomplexed peptide, the addition of the hydrophobic −LLA group clearly results in a larger reduction in tension from the clean interface value for all concentrations. At the same bulk concentration, the tensions of solutions of LBT^{3-} are lower than those of LBT^{5-}; this may be attributed to the reduced charge of LBT^{3-}, which shifts the molecule's hydrophilic–hydrophobic balance and reduces electrostatic repulsion in the interface, favoring adsorption.

To characterize the surface tension of LBT:Tb^{3+}-laden interfaces, solutions were prepared with LBT to Tb^{3+} ratio of 1:4 to drive nearly complete complexation. For all three variants, the quasi-equilibrium surface tension is reduced relative to the uncomplexed form at all peptide concentrations studied. This finding indicates that the complexed form is more surface active and adsorbs to a higher concentration than the uncomplexed form. This increase in surface activity can be attributed to two effects. First, LBT:Tb^{3+} complexes have lower net charge relative to their uncomplexed forms. The reduction in charge shifts their hydrophobic–hydrophilic balance and reduces their electrostatic repulsion so that more can adsorb at the interface. Second, the compact complex occupies a lower molecular surface area than the uncomplexed peptide, allowing a greater number of complexed species to adsorb relative to the uncomplexed form. The difference in surface tension reduction between bound and unbound species is approximately 5%, 17%, and 2% for LBT^{5-}, LBTLLA^{5-}, and LBT^{3-}, respectively. The strong change for LBTLLA^{5-} indicates that the additional hydrophobic residues generate higher surface activity even in the bound state. As a consequence of the fact that the LBT layers are not in thermodynamic equilibrium with the bulk, the surface concentration of the peptides cannot be determined from the measurements of the tension as a function of the bulk concentration and the Gibbs adsorption equation, as has been recognized in the study of protein layers which are also not in equilibrium (71). XR measurements provide values for the surface concentrations of the LBTs in the interfacial layer, and provide additional insight into the trends observed in the tension measurements. XR measurements of surface concentrations of insoluble fatty acids, where the surface concentrations are known, provide verification of this technique (e.g., ref. 72). In addition, X-ray excited fluorescence of Tb^{3+} near total reflection (XFNTR) allows the direct measurement of the cation surface concentration which, alongside the reflectivity, provides a complete picture of the peptide and cation adsorption at the surface.

XR/XFNTR Measurements of Adsorbed Layers of LBT and LBT:Tb^{3+}. The surface concentrations of the LBT peptides adsorbed from solution to an air/water interface were obtained by directing X-rays (wavelength λ, of 1.24 Å) at grazing incidence to the planar interface of a liquid layer of the peptide solutions in rectangular troughs with millimetric depths, and recording the intensity of the specular reflection ($\mathcal{R}$) at different incident angles (α) (73) (*Materials and Methods*). XR measurements are

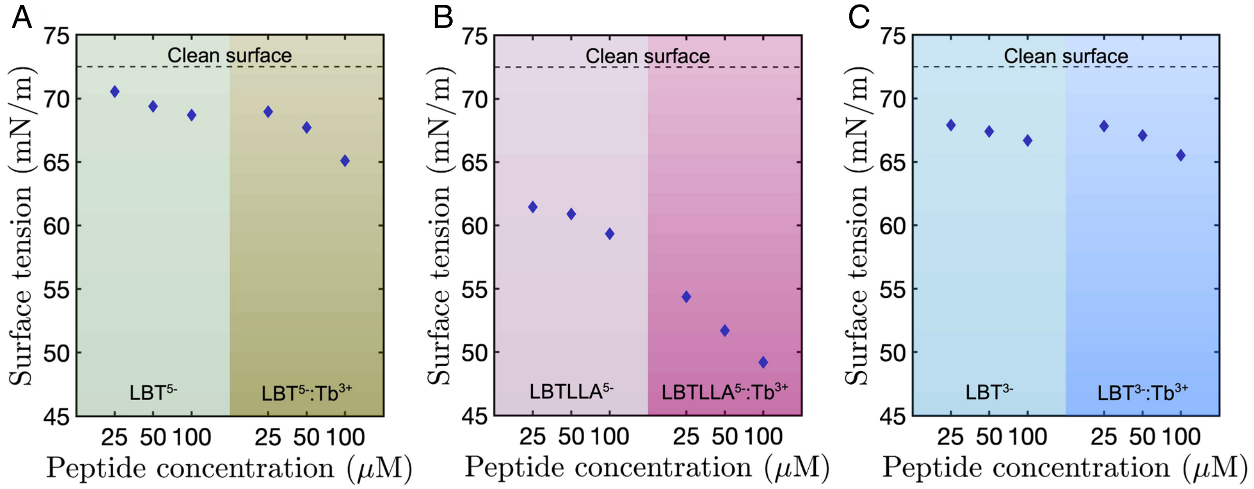

Fig. 2. Quasi-equilibrium surface tension measurements, at different bulk concentrations of LBT peptides in the absence and presence of Tb^{3+} at a ratio of LBT:Tb^{3+} equal to 1:4, for (*A*) LBT^{5-} and LBT^{5-}:Tb^{3+}, (*B*) LBTLLA^{5-} and LBTLLA^{5-}:Tb^{3+}, and (*C*) LBT^{3-} and LBT^{3-}:Tb^{3+}. Tension measurements are obtained in triplicate with SD ± 0.5 % or less; error bars are plotted but too small to be visible.

formulated as reflectivity relative to the Fresnel reflectivity ($\mathcal{R}_F$) from an ideally smooth air/water interface, i.e., $\mathcal{R}/\mathcal{R}_F$, as a function of the wave vector transfer $Q_z = (4\pi/\lambda)sin(\alpha)$. The specular reflection is fit to slab models (*SI Appendix*, Fig. S2) of the electron density profile (EDP, $\rho(z)$) normal to the interface with each slab of thickness d_i and thermal interfacial roughness σ having a uniform density ρ_i (74). By integrating the EDP through the layer, the surface concentrations Γ_{LBT} can be obtained by accounting for the known number of electrons from all species at the interface and their partial molar volumes (*SI Appendix*). Errors in the fitted parameters are obtained by mapping the chi-squared space (square deviation between the reflectivity measurement and fit for a given parameter set d_i, ρ_i and σ) which allows an assignment of the errors in the calculated surface concentrations.

The fluorescence of the Tb^{3+} in the interfacial layers is also measured, excited directly by the low angle incident X-rays irradiating the air/water surface (*Materials and Methods*). The measurements are taken at angles (values of Q_z) near the critical angle α_c for total external reflection, and the excitation through the layer and into the bulk liquid is in the form of an exponentially decaying wave passing through the interface for angles less than the critical angle. The spectrum of the fluorescence (*SI Appendix*, Fig. S3) is measured by a detector above the trough, and the integrated intensity of the strongest line of the Tb^{3+} (or La^{3+}) fluorescence ($\mathcal{L}_\alpha$) is obtained for each of the values of Q_z near the critical value. Fluorescence measurements from a solution without peptide and with a known concentration of cation are used to measure a calibration coefficient (*SI Appendix*, Fig. S4). The surface concentration of cations ($\Gamma_{Tb^{3+}}$) is then obtained by fitting the adsorbed species intensity as a function of Q_z with the calibration coefficient that scales the fluorescence (75); mapping of the error in the coefficient, as with the XR data, allows error bars to be assigned to the surface measurement (74). With the surface concentration determined, the electron and molar volume balances become closed, and the surface concentrations of the peptide can be calculated (see *SI Appendix* for details of the calculations).

Absent Tb^{3+}, the normalized reflectivity $\mathcal{R}/\mathcal{R}_F$ increases with concentration for adsorbed layers at interfaces of LBT solutions at concentrations 25, 50, and 100 µM, as reported in *SI Appendix*, Fig. S6 *A–C* for each variant. This increase indicates, as expected, a greater adsorption with increasing bulk concentration. The EDPs ($\rho(z)$), derived from the slab model, are reported in Fig. 3 *A–C*; Parratt fitting required three slabs; the fitting parameters are given in *SI Appendix*, Table S1. For each variant, over this range of concentrations, the thickness of the layer varies

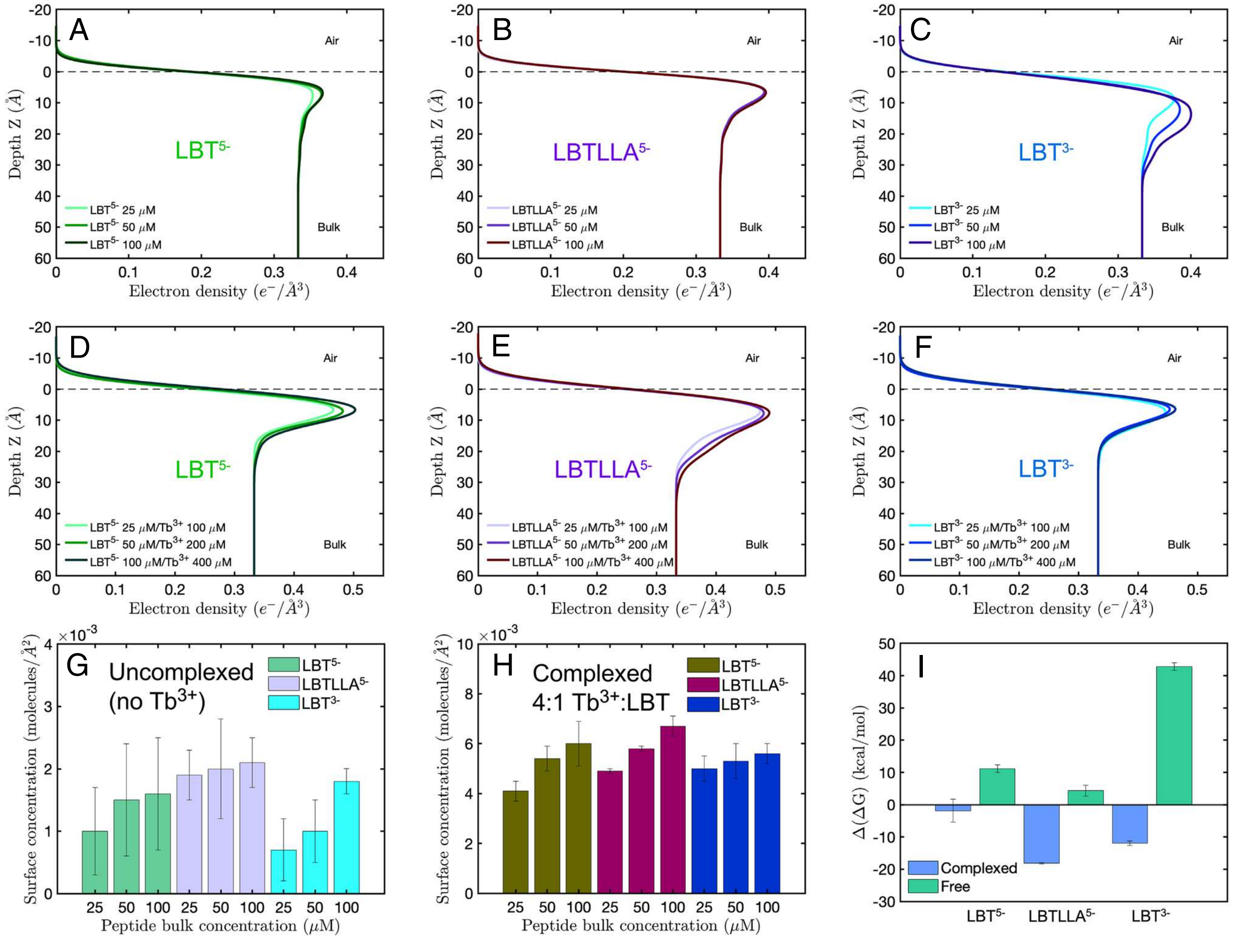

Fig. 3. Electron density profiles of the interfacial layers for LBT^{5-}, $LBTLLA^{5-}$ and LBT^{3-} at the air/water interface adsorbed from solutions of 25, 50, and 100 µM LBT without Tb^{3+} (*A–C*) and with cations (*D–F*) in a 1:4 ratio of LBT to Tb^{3+}. The horizontal dashed lines separate the air phase from the liquid phase at the interface. (*G* and *H*) Interfacial concentration of LBT^{5-}, $LBTLLA^{5-}$ and LBT^{3-} as a function of peptide bulk concentration in the absence (*G*) and presence (*H*) of Tb^{3+} cations at a ratio LBT:Tb^{3+} of 1:4. (*I*) Free energy of adsorption of peptides to the air–aqueous interface from a bulk aqueous solution. The blue bars represent the peptides forming a complex with Tb^{3+}, whereas the green bars are for ion-free peptides.

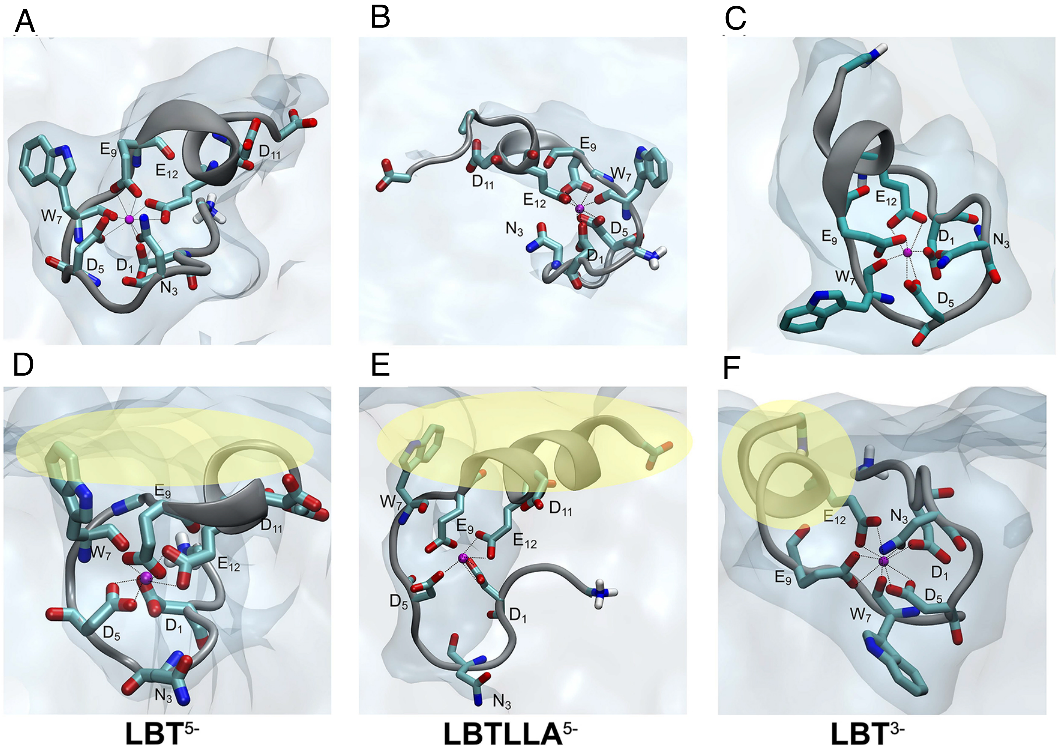

Fig. 4. MD simulations of single LBT: Tb^{3+} complexes adsorbing to the interface. (*A*–*C*) are the bulk structures for LBT^{5-}, LBTLLA^{5-} and LBT^{3-} ("initial" microsecond simulations for simulations at the surface). At the interface, LBT^{5-} reconfigures to the conformations in (*D*); LBTLLA^{5-} to (*E*) and LBT^{3-} reconfigures to (*F*). The dotted lines in the coordination loop indicate peptide-oxygen cation distances less than or equal to 0.25 nm. Yellow circles are used to highlight the residues close to the air phase at the interface.

from $\approx$ 25 to 35 Å (*SI Appendix*, Table S1). The surface concentrations of the peptides (Γ_{LBT}) are reported in Fig. 3*G* and surface concentration of water molecules is reported in *SI Appendix*, Fig. S5. For each LBT, Γ_{LBT} increases with the bulk concentration, consistent with the trends in quasi-equilibrium surface tensions with concentration (Fig. 2). Note that the change in surface concentration is not directly proportional to the change in surface pressure. This discrepancy is likely due to the uncomplexed molecules adopting a linear configuration at the interface, as shown in the simulated structures in *SI Appendix*, Fig. S7. This organization may lead to stacking and increased adsorption without a corresponding significant increase in surface tension. At each concentration, LBTLLA^{5-} displayed the largest reduction in tension and correspondingly the highest surface concentrations.

To characterize the adsorption of LBT:Tb^{3+} complexes, reflectivities $\mathcal{R}/\mathcal{R}_F$ were measured for fixed LBT to Tb^{3+} ratio of 1:4 for all variants, as was done previously for the surface tension measurements (Fig. 2). The reflectivity data are reported in *SI Appendix*, Fig. S6 *D*–*F*. The corresponding EDPs and are given in Fig. 3 *D*–*F*. The slab model fitting parameters (d_i and ρ_i) are given in *SI Appendix*, Table S2. Here, the Parratt fitting involves only two slabs, owing to the compact configuration of peptide within the LBT:Tb^{3+} complexes, and the values of d_i indicate only monolayer coverage of the complexed form. While the maximum value of the electron density is approximately the same for complexes of all three variants, the distribution of the electron density along the interfacial zone ($e^-/\text{Å}^3$) is greatest for the LBTLLA^{5-}:Tb^{3+}-laden interfaces. Additionally, these layers are up to 8 Å thicker than LBT^{5-}:Tb^{3+} and LBT^{3-}:Tb^{3+}; this difference can be attributed to the relatively higher surface coverage of the more hydrophobic complexes. Last, for each variant, the EDP along z for complex–laden interfaces (Fig. 3 *D*–*F*) are greater than the corresponding EDPs absent Tb^{3+} (Fig. 3 *A*–*C*). This trend is consistent with higher interfacial densities of LBT:Tb^{3+} complexes attributed to their relatively weak electrostatic repulsion and compact conformations. The surface concentration of water molecules is reported in *SI Appendix*, Fig. S8.

The surface concentrations determined for each variant in LBT:Tb^{3+} complexes, reported in Fig. 3*H*, show that Γ_{LBT} increases with bulk concentration. As expected, the hydrophobic LBTLLA^{5-}:Tb^{3+} has the largest surface concentration at all three bulk concentrations. Furthermore, as anticipated from the raw EDPs, at each bulk concentration of a LBT, Γ_{LBT} of the complexed form is larger than the uncomplexed form for all variants.

Fig. 4 *D*–*F* show conformations of single LBT:Tb^{3+} complexes at the air/water interface from MD simulations for each variant. To perform these simulations, LBT:Tb^{3+} conformations obtained after microsecond simulations (Fig. 4 *A*–*C*) were placed near the interface and allowed to adsorb and reconfigure/equilibrate at the interface for approximately a microsecond until steady coordination is observed. MD simulations of the conformations of single LBT:Tb^{3+} in aqueous solution were undertaken using the LBT^{5-} crystallographic structure (Fig. 1*A*) as a starting point (*Materials and Methods*). All complexes show compact structures with a shell of coordinating residues wrapping around the Tb^{3+}, consistent with X-ray crystallographic data. Importantly, the MD simulations at the surface indicate that the cation is retained in the binding loop as the complex adsorbs, and that the coordinating loop when exposed to the surface remains intact. Fig. 4 clearly shows that the hydrophobic residues at the C-terminus, i.e., −LLA for $\mathrm{LBT^{5-}}$ and $\mathrm{LBT^{3-}}$, and −LLALLA for $\mathrm{LBTLLA^{5-}}$, locate near the interface and account for the surface activity of the $\mathrm{LBT{:}Tb^{3+}}$ complexes (see yellow circled residues). The tryptophan residue also typically locates at the interface to contribute to the amphiphilic character.

The change in the free energy ($\Delta\Delta G$) between the molecules in bulk solution (Fig. 4 *A*–*C*) and at the air–aqueous interface (Fig. 4 *D*–*F*) is calculated from the MD simulations and is shown in Fig. 3*I* from the algorithm discussed in *SI Appendix*, Eqs. **S1** and **S2**. As expected, absent $\mathrm{Tb^{3+}}$, the hydrophobic $\mathrm{LBTLLA^{5-}}$ has the lowest change of free energy among the three variants, with ranking $\mathrm{LBTLLA^{5-}<LBT^{5-}<LBT^{3-}}$. All three variants are more surface active when complexed to $\mathrm{Tb^{3+}}$, in agreement with the experimental results. Upon complexation, peptides will migrate to the interface with the trivalent ion. The calculations reveal that the complex formed by $\mathrm{LBTLLA^{5-}}$ is most hydrophobic, with free energy change upon adsorption ranked $\mathrm{LBTLLA^{5-}{:}Tb^{3+}<LBT^{3-}{:}Tb^{3+}<LBT^{5-}{:}Tb^{3+}}$.

Thus far, experiment has demonstrated that LBTs retain their selectivity profile in bulk solution even when their sequences are amended to make variants with greater hydrophobicity or reduced net charge. All three LBT variants are surface active absent $\mathrm{Tb^{3+}}$, and more surface active when complexed to $\mathrm{Tb^{3+}}$. MD simulations show that the LBT variants capture $\mathrm{Tb^{3+}}$ in bulk, and retain the bound $\mathrm{Tb^{3+}}$ upon adsorption. In order to develop LBTs as selective surfactants for REE capture at air–aqueous interfaces, it is important to quantify the number of cations per peptide at the interface.

The independent XFNTR measurements of the surface concentration of $\mathrm{Tb^{3+}}$ performed for the 1:4 peptide to cation molar ratio are given in *SI Appendix*, Fig. S9 as calculated from the integrated fluorescence under the L_α line as a function of Q_z (*SI Appendix*, Fig. S3). From the XR measurements of Γ_{LBT}, the ratio LBT to cation ($\chi = \Gamma_{Tb^{3+}}/\Gamma_{LBT}$) can be calculated and is given in Fig. 5*A*. The χ values at the different subphase concentrations show that for $\mathrm{LBT^{5-}}$ and $\mathrm{LBTLLA^{5-}}$, χ is approximately between 1.7 and 1.9, and for $\mathrm{LBT^{3-}}$, χ is approximately 1. While each LBT complexes one cation in its binding loop, the adsorption of excess $\mathrm{Tb^{3+}}$ observed for $\mathrm{LBT^{5-}}$ and $\mathrm{LBTLLA^{5-}}$ interfacial layers is not surprising. $\mathrm{LBT^{5-}{:}Tb^{3+}}$ and $\mathrm{LBTLLA^{5-}{:}Tb^{3+}}$ complexes with a cation in the binding loop are negatively charged (net charge of −2). Thus, an adsorbed layer containing these complexes would be negatively charged and would attract free trivalent cations in the underlying media via nonselective Coulombic interactions. These cations would reduce the surface charge, providing an excess of cations relative to peptide. In the case of $\mathrm{LBT^{3-}}$, the complexed peptide is uncharged and excess $\mathrm{Tb^{3+}}$ is not recruited to the interface.

To understand more clearly this nonspecific electrostatic binding and whether excess cations can bridge different $\mathrm{LBT^{5-}}$ and $\mathrm{LBTLLA^{5-}}$ complexes, MD simulations are undertaken of the interfacial layer. In these simulations, LBTs are equilibrated individually in the bulk in microsecond simulations from the crystallographic starting point as before (Fig. 4 *A*–*C*), and are then placed as a layer at the interface and allowed to equilibrate at the surface as in Fig. 4 *D*–*F* to form stable interfacial layers. This equilibration/reconfiguration is followed for one microsecond. The surface concentration of the LBTs placed at the surface was selected based on the XR results, Fig. 3*H*. $\mathrm{Tb^{3+}}$ cations are placed in the bulk so that the ratio of these cations to the LBT (including the complexed cations) is four to one, and the system is made neutral with the addition of $\mathrm{Na^{+}}$, $\mathrm{Cl^{-}}$ and the MES buffer as in the case of the LBT simulations of single complexed peptides. The last 400 ns of the one-microsecond MD trajectories are used to study the number of adsorbed $\mathrm{Tb^{3+}}$ cations per peptide molecule at the interface. A ratio of $\mathrm{Tb^{3+}}$ to peptide close to 2 at the interface for $\mathrm{LBT^{5-}}$ and $\mathrm{LBTLLA^{5-}}$ (Fig. 5*B*) was obtained for all the different molecular areas at the interface, quantitatively in agreement with Fig. 5*A* and validating the hypothesis that extra unbound $\mathrm{Tb^{3+}}$ in solution can adsorb to the air–aqueous interface for the negatively charged complexes $\mathrm{LBT^{5-}}$ and $\mathrm{LBTLLA^{5-}}$ to neutralize the charge. For $\mathrm{LBT^{3-}}$, a ratio of approximately one is obtained, also in agreement with experiments indicating no excess charge.

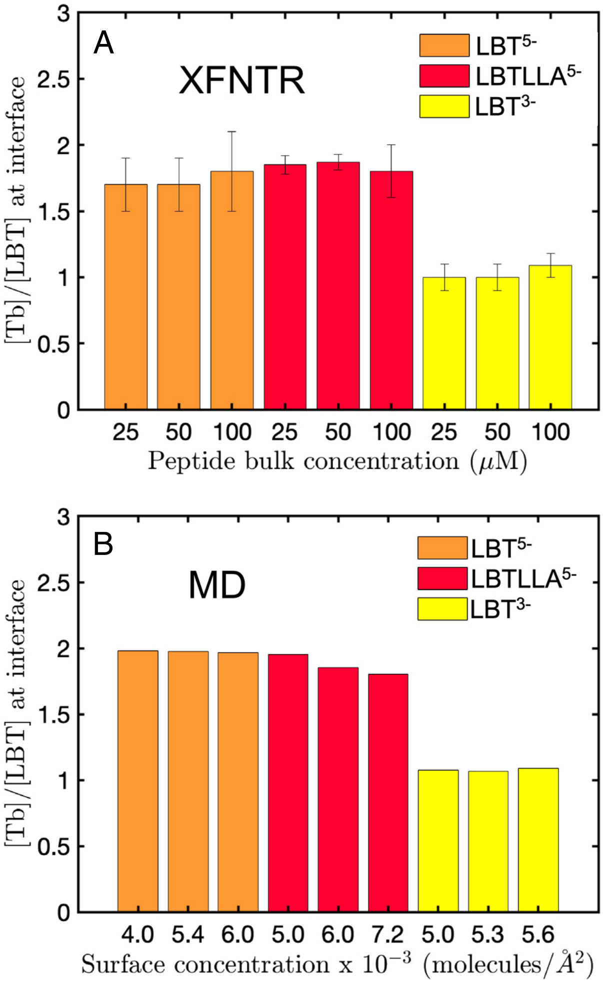

Fig. 5. Number of $\mathrm{Tb^{3+}}$ per LBT peptide in the interfacial zone for different bulk concentrations of peptide and $\mathrm{Tb^{3+}}$ cations at a ratio $\mathrm{LBT{:}Tb^{3+}}$ 1:4 from XFNTR (*A*) and MD simulation (*B*).

Snapshots of a normal view of a highly populated interface $\mathrm{LBTs^{5-}{:}Tb^{3+}}$ ($\mathrm{LBT^{5-}}$ and $\mathrm{LBTLLA^{5-}}$) complexes and $\mathrm{Tb^{3+}}$ associating with these complexes are shown in Figs. S10a, and S10b. The snapshots show that $\mathrm{Tb^{3+}}$ cations outside the binding pocket coordinate with the carboxylate groups from the residue D11 and the C-terminus of the peptides. Moreover, a bridge forms between two $\mathrm{LBTs^{5-}{:}Tb^{3+}}$ when $\mathrm{Tb^{3+}}$ ions associate with carboxylate groups of different molecules as in *SI Appendix*, Fig. S10 *A* and *B*. Reduction in the net charge of the peptide

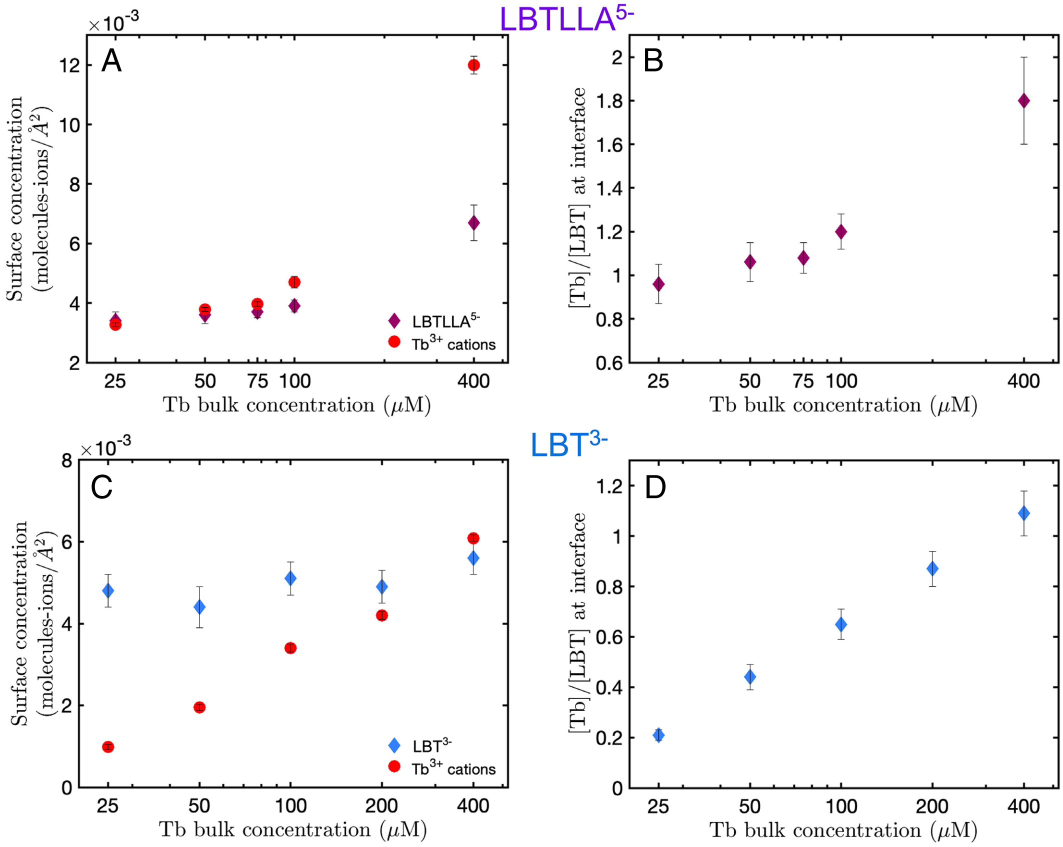

Fig. 6. XR and XFNTR measurements of adsorption of LBT and Tb^{3+} at the air/water interface from solutions with a fixed 100 μM concentration of peptide: (*A*) interfacial concentration of $LBTLLA^{5-}$ and Tb^{3+} cations at different bulk concentrations of Tb^{3+} and (*B*) the cation to LBT ratio at the interface, (*C*) interfacial concentration of LBT^{3-} and Tb^{3+} cations at different bulk concentrations of Tb^{3+} and (*D*) the cation to LBT ratio at the interface.

(LBT^{3-}) to form neutral complexes dramatically changes the nature of the interfacial structure. Interfacial films formed from LBT^{3-} in the presence of excess Tb^{3+} have approximately one Tb^{3+} ion per molecule (shown in Fig. 5*B*, yellow bars). Furthermore, for LBT^{3-}:Tb^{3+} complexes simulation reveals that only the ions that form the complex with the peptide adsorb to the interface. This result is consistent with the experimental results and confirms that for the peptide LBT^{3-}, Tb^{3+} ions are adsorbed to the interface only via charged groups that form the selective binding loop as shown in the snapshot of the interfacial film in *SI Appendix*, Fig. S10*C*.

To examine how such bridging by excess Tb^{3+} alters peptide adsorption, interfacial XR and XFNTR measurements were performed of solutions $LBTLLA^{5-}$ at 100 μM with Tb^{3+} concentrations varying from 25 to 400 μM (saturation). The normalized reflectivity measurements $\mathcal{R}/\mathcal{R}_F$ for interfacial layers, corresponding EDPs, and integrated Tb^{3+} fluorescence are given in *SI Appendix*, Fig. S11 and Table S3 contains the fitting parameters for the XR data. The surface concentration of water molecules is reported in *SI Appendix*, Fig. S12. The interfacial concentration of peptide (Fig. 6*A*) increases marginally with added Tb^{3+} up to equimolar concentrations. However, as the Tb^{3+} bulk concentration approaches saturation (i.e., 4:1 bulk cation to peptide concentrations), adsorption of $LBTLLA^{5-}$ dramatically increases (Fig. 6*A*) indicating that electrostatic bridging recruits $LBTLLA^{5-}$ to the surface. The number of Tb^{3+} cations per adsorbed peptide is shown in Fig. 6*B*. For the lowest concentration of Tb^{3+} (25 μM) the ratio is 0.96 ± 0.09, which indicates that although the peptide is not saturated, only bound species are populating the interface and the number of unbound Tb^{3+} in solution are not sufficient to coordinate with the negatively charged group outside the binding loop. For higher concentrations of Tb^{3+} the ratio increases until the maximum is reached at a concentration of 400 μM of trivalent cations (see also Fig. 5*A*). Thus, free Tb^{3+}, in large excess, can associate with the negatively charged groups of the peptide outside of the binding loop to recruit peptide to the surface and to achieve a ratio of 1.8 (Tb^{3+}:$LBTLLA^{5-}$).

Similar interfacial XR and XFNTR measurements were performed on LBT^{3-}, which does not promote a secondary binding. The peptide concentration was again fixed at 100 μM and the Tb^{3+} concentrations varied from 25 to 400 μM (saturation). The normalized reflectivity measurements $\mathcal{R}/\mathcal{R}_F$ for interfacial layers, corresponding EDPs, and integrated Tb^{3+} fluorescence are given in *SI Appendix*, Fig. S13 and Table S4 contains the fitting parameters for the XR data. The surface concentration of water molecules is reported in *SI Appendix*, Fig. S14. Fig. 6*C* shows that as the bulk concentration of Tb^{3+} increases, the LBT^{3-} surface concentration increases only marginally when Tb^{3+} bulk concentrations are greater than equimolar, presumably because the subphase contains increasing concentrations of the more surface active complexed form. However, unlike $LBTLLA^{5-}$, there is no evidence of excess cation-enabled recruitment of extra, complexed, peptides that yielded the much larger increase in adsorbed peptide concentration for $LBTLLA^{5-}$. The ratio of $\Gamma_{Tb^{3+}}/\Gamma_{LBT^{3-}}$ (reported in Fig. 6*D*), increases to unity as the surface transitions from a mixed layer of uncomplexed and complexed peptide to a layer of completely complexed peptide.

Selectivity at Interfaces: Competitive Adsorption of LBT^{3-}:Tb^{3+} and LBT^{3-}:La^{3+} Complexes. We have shown that LBT^{3-} complexes REEs in bulk, retains the cation in its binding loop upon adsorption, and recruits only one REE cation per peptide, without nonselectively bound REE that might compromise selective cation capture. We now study LBT complexation and adsorption of REE cations from mixed aqueous feedstocks to identify factors that influence selectivity at the interface. Solutions were prepared containing 100 μM LBT^{3-} with equimolar mixtures of two lanthanides, terbium (Tb^{3+}) and lanthanum (La^{3+}). The equimolar mixtures varied in total lanthanide concentration from 50 µM in which the LBTs would be partially complexed to 1,000 µM, an upper "saturation" limit in which all the LBTs would be complexed. The lanthanum cation was chosen because in the bulk, La^{3+} has less affinity than Tb^{3+} for the LBTs (see the K_Ds from fluorescence measurements in Fig. 1 *C*–*E*). The fluorescence of La^{3+} was determined by the same methods as described above for Tb^{3+}; XR and XFNTR studies were performed. The XR and XFNTR data and the electron density profiles in *SI Appendix*, Fig. S15 and Table S5. The surface concentration of water molecules is reported in *SI Appendix*, Fig. S16. The surface concentrations (*SI Appendix*, Fig. S17*A*) shows, as with LBT^{3-}:Tb^{3+}, that the ratio of La^{3+} to LBT is approximately 1, as the uncharged complex LBT^{3-}:La^{3+} does not bridge, as was found for LBT^{3-}:Tb^{3+}.

The resulting interfacial compositions reveal a complex selectivity profile at the interfaces that differs significantly from that in the bulk. The ratio of the total adsorbed lanthanide cations to adsorbed peptides (Fig. 7*A*) increases with bulk lanthanide concentration to approach a value of unity at elevated cation concentration. This adsorbed layer likely contains primarily complexed LBT:REE at the surface. In this layer, the ratio of Tb^{3+} to La^{3+} increases from approximately 0.25 for 50 µM total Ln^{3+} to 2.0 at the highest total concentration (1,000 µM); see Fig. 7*B*. The interface is selective for La^{3+} at low REE concentration, and selective for Tb^{3+} at high concentration. At the very low concentration (<200 µM) the enrichment in La^{3+} can be attributed to the faster adsorption kinetics and greater surface activity of the LBT^{3-}:La^{3+} complex relative to the LBT^{3-}:Tb^{3+} complex, as supported by dynamic surface tension data (*SI Appendix*, Fig. S20*A*) and the lower quasi-equilibrium surface tension values for the LBT^{3-}:La^{3+} (*SI Appendix*, Fig. S20*B*). MD simulations of the complexes in solution (*SI Appendix*, Fig. S21 *A* and *B*) reveal a more open binding pocket for the LBT^{3-}:La^{3+} complex compared to the LBT^{3-}:Tb^{3+} complex. This more open conformation, likely responsible for the lower affinity of the peptide for La^{3+} over Tb^{3+}, may result in greater exposure of hydrophobic regions, contributing to the higher surface activity observed for the LBT^{3-}:La^{3+} complex relative to the LBT^{3-}:Tb^{3+} complex. *SI Appendix*, Fig. S22 shows that the energy of adsorption for the La^{3+}-complexed peptide is lower over the Tb^{3+} one, in agreement with the more hydrophobic groups of this complex which drives a high surface activity. MD simulations of the LBT^{3-}:Tb^{3+} and LBT^{3-}:La^{3+} complexes over a 3,000 ns timescale reveal that the mean square displacement (MSD) in bulk solution is consistently higher for the LBT^{3-}:La^{3+} complex compared to the LBT^{3-}:Tb^{3+} complex (*SI Appendix*, Fig. S23). The higher MSD suggests that the LBT^{3-}:La^{3+} complex exhibits greater diffusive motion, which correlates with a higher diffusion coefficient. This enhanced diffusion allows for faster transport of the LBT^{3-}La^{3+} complex to the air–water interface, contributing to its faster adsorption kinetics, as observed in experimental results. In contrast, the lower MSD for the LBT^{3-}:Tb^{3+} complex indicates slower diffusion in the bulk phase, which likely results in delayed adsorption to the interface. At higher concentrations, the surface becomes enriched in Tb^{3+}. In this regime, the peptide binding loops in the bulk become saturated with Tb^{3+} because of the much lower dissociation constant and the surface becomes enriched in the bulk dominant LBT^{3-}:Tb^{3+} complex. From the bulk dissociation constants K_D for Tb^{3+} and La^{3+} measured (Fig. 1*E*) for LBT^{3-}, the ratio of Tb^{3+} to La^{3+} should be 24.8 for a equimolar mixture of Tb^{3+} and La^{3+} with a total concentration 1,000 µM. The observed value, approximately 2, is 10 times less. This difference can arise from the fact that the surface environment of the adsorbed peptide, with exposure to the air phase, can result in changes in the binding loop conformation at the interface

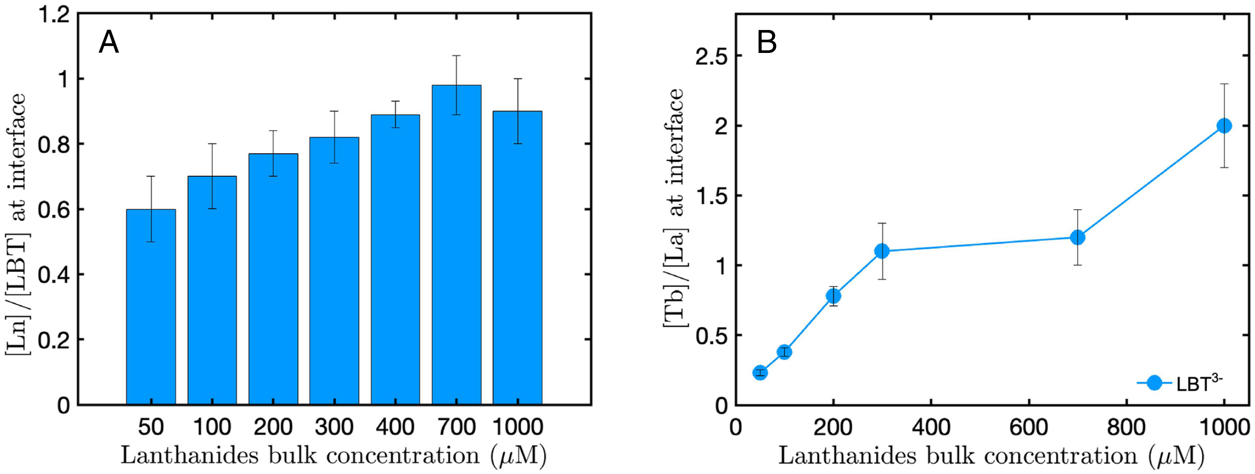

Fig. 7. XR and XFNTR measurements of competitive adsorption to the air/water interface from equimolar mixtures of Tb^{3+} and La^{3+} in 100 μM solutions of LBT^{3-}: (*A*) ratio of total lanthanide ion concentration to LBT and (*B*) ratio of Tb^{3+} to La^{3+} at the interface for different total bulk concentrations of the 1:1 mixture of cations as a function of total lanthanide bulk concentration.

to a conformation, as indicated by MD simulated structures adsorbed to the air–water interface (*SI Appendix*, Fig. S24), which might favor La^{3+} which forms the more surface active complex. Additionally, the fluorescence spectroscopy measurements of K_D in the bulk are undertaken at concentrations (order 100 nM) much lower than those of the tension and XR and fluorescence experiments (order 100 μM). At these higher concentrations (necessary to achieve significant adsorption onto the air/water interface) the peptides tend to aggregate in complex oligomers that can influence the dissociation constants and surface activity of the peptide structures. Future directions which aim to retain the selectivity achieved at low concentrations of LBTs where the peptides are isolated suggest that the LBTs can be hosted on platforms or supports which space the peptides apart so that their low bulk concentration isolated selectivity can be retained. The challenge in this case is to attach the peptides so that the binding loop is functional and the support can be recovered in a foam recovery, e.g., nanoparticles that are surface-modified to be surface active as in Ye et al. (44) who attached lanmodulin to magnetic particles for a magnetic separation. Alternatively, an LBT which upon complexation to a particular lanthanide becomes strongly hydrophobic can selectively deliver the cation to the air/water interface utilizes directly surface activity for separation. LBT-surfactant-based REEs separation schemes could be developed to exploit these effects, and will be the focus of future work.

Materials and Methods

Materials. LBT^{5-}: YIDTNNDGWYEGDELLA (purity 98%), $LBTLLA^{5-}$: YIDTNNDGWYEGDELLALLA (purity ≥95%) both labeled at the N-terminus with a free amine and labeled at the C-terminus with a free acid, and LBT^{3-}: YIDTNNDGWYEGNELLA (purity ≥95%) labeled at the N-terminus with a free amine and at the C-terminus with an amide, were purchased from GenScript (Piscataway, NJ), diluted to a stock concentration of 300 μM in buffer solutions containing 100 mM of NaCl (purity ≥99.5%, Sigma-Aldrich) and 50 mM of MES (purity ≥99.5%, Sigma-Aldrich) at a pH of 6, and used without additional purification. $TbCl_3$ hexahydrate (purity ≥99.999%) and $LaCl_3$ heptahydrate (purity ≥99.999%) were purchased from Sigma-Aldrich and diluted to a stock concentration of 25 mM in the same buffer solution containing 100 mM of NaCl and 50 mM of MES. Buffer solution is filtered using a 0.22 μm polytetrafluoroethylene filter. Ultrapure water is obtained from a Milli-Q water filtration unit (EMD Millipore) with a resistivity of 18.2 mΩ-cm and used for preparation of buffer solution.

Luminescence Spectroscopy. Energy transfer between Tryptophan (Trp) (position 7, for all peptides) and Tb^{3+} was monitored with a Tecan Spark plate reader, using a 96-well plate in triplicate. Trp was excited at 280 nm and emission spectra were detected at 545 nm. As the concentration of Tb^{3+} increases in solution for a constant concentration of peptide, the collected emission became more intense until the luminescence intensity became constant (maximum value for saturation of peptide). The collected data were fitted to produce thermodynamic parameters for the association of the peptide with Tb^{3+}. To obtain thermodynamic association parameters for the rest of the series of lanthanides, displacement assays were carried out. Tb^{3+} cations were added to the peptide solution, followed by increasing amounts of other Ln^{3+}. As more of the other Ln^{3+} was added, Tb^{3+} was displaced. The other lanthanides do not emit at 545 nm, so this displacement promoted a reduction in detected luminescence, that allowed to determine binding free energy and affinity constants for the rest of the Ln^{3+} series one at the time.

Surface Tension Measurements. Dynamic surface tensions at the air/aqueous interface were measured using a pendant drop tensiometer (Attension Theta, Biolin Scientific, Stockholm, Sweden). Solutions were prepared with different concentrations of LBT and Tb^{3+} and 14 μL drops of these solutions were formed and suspended from a 16-gauge metal needle. An optical train forms images of the silhouette of the hanging drop which are captured by a camera; fitting of the drop contour with solutions of the Young Laplace equation allows the surface tension of the drop to be calculated. The drop is formed impulsively and the peptide and complex adsorb to the clean surface; images of this process captured over time measure the dynamic tension.

Liquid Surface X-Ray Measurements. XR and XFNTR were measured at NSF's ChemMatCARs, sector 15-ID-C experimental hutch at the Advanced Photon Source in Argonne National Laboratory (Lemont, IL) using 10 keV X-rays. The liquid sample was placed in a trough of maximum surface area of 21 cm^2 within the XR apparatus at 15-ID-C. The trough was filled with approximately 6 mL of solutions of LBTs or LBTs:Ln^{3+}. The trough was contained in a sealed aluminum box, resting on a vibration isolation table. After the trough was filled, the box was closed. A slight overpressure of helium was kept in the box to reduce X-ray background scattering. All measurements were taken after approximately 2 h of the filling process and equilibration at room temperature. The photon flux was adjusted using absorbers placed before the sample to prevent beam damage. An XR scan took 40 min, while an XFNTR scan took 15 min. Beam damage was evaluated by repeating the experiments with a representative sample, and the consistent results confirmed that the sample integrity remained intact throughout the measurements, indicating no beam-induced alterations to the interfacial structure.

XR. XR measures the interfacial electron density profile. XR data were measured as a function of wave vector transfer $Q_z = (4\pi/\lambda)\sin(\alpha)$ along the surface normal to cover the range $0.016\ \text{Å}^{-1} < Q_z < 0.6\ \text{Å}^{-1}$, where α is the angle of incidence and λ is the X-ray wavelength $\lambda = 1.24$ Å. XR data were measured with a Pilatus 200K area detector. Reflectivity was measured multiple times to check for stability. XR measurements were fit to a model functional form to compute the electron density $\rho(z)$ along the z direction perpendicular to the interface, and averaged over the x–y plane of the surface, with the model function represented by a sum of error functions (73):

$$\rho(z) = \frac{1}{2}\sum_{i=0}^{N-1} \mathrm{erf}\left(\frac{z - z_i}{\sqrt{2}\sigma}\right)(\rho_i - \rho_{i+1}) + \frac{\rho_0 - \rho_N}{2} \qquad [1]$$

with $\mathrm{erf}(z) = (2/\sqrt{\pi})\int_0^z e^{-t^2}dt$; N the number of internal interfaces within the surface film, σ the interfacial roughness, ρ_0 the electron density of the bulk aqueous phase, ρ_N the electron density of the air phase, ρ_i and z_i the electron density and the position of the i^{th} slab and interface, respectively. The thickness of the i^{th} slab, d_i, is defined as $|z - z_i|$. XR was computed using the Parratt formalism by discretizing the electron density profile (EDP) from Eq. **1**. XR measurements were normalized to the Fresnel reflectivity R_F, which is calculated for a theoretical liquid–air interface where the electron density varies as a step function between the two bulk phases (73).

XFNTR. XFNTR measures the surface number density of fluorescing metal ions (number per Å^2). X-ray fluorescence intensity was measured for a range of Q_z near the critical value Q_c for total reflection. The X-ray fluorescence spectrum was measured by a Vortex-90-EX silicon drift detector placed above the interface and spectra were normalized to the incident beam intensity. The XFNTR signal was obtained by integrating the fluorescence peak of Ln^{3+} over the acceptance volume in the aqueous phase, as described in detail in Supporting Information and in previous work (75, 76).

MD Simulations. MD simulations are performed to model the uncomplexed and the LBT:Tb^{3+} binding complex in aqueous solution using GROMACS package (77, 78). All peptides were modeled using CHARMM36 force field (79). Terbium cation was modeled using the modified CHARMM force field (80), which was designed to match the hydration structure and hydrogen free energy from experimental measurements. The solvent was modeled using the modified Tip3p water model under neutral pH condition. Unless differently stated, we use periodic boundary conditions in the x-, y-, and z-directions. Sodium and chloride ions were used to neutralize the system and the concentration of NaCl was 100 mM, which is comparable to the experimental conditions (80). Particle Mesh Ewald algorithm (81) was adopted for the calculation of long-range electrostatic interactions. The integration time step was set to 2.0 fs, and the LINCS algorithm (82) was employed to constrain the lengths of all chemical bonds involving hydrogen atoms at their equilibrium values. The initial configuration of the LBT^{5-}:Tb^{3+} binding complex was obtained from the X-ray measurements [PDB code: 1TJBI (35)]. The solvated system was first energy minimized using the Steepest Descent (SD), while algorithms were used to remove unfavorable contacts. The isochoric isothermal (NVT) simulation were then performed at room temperature of 298 K using a stochastic velocity rescaling algorithm for 5 ns (83). After the equilibration stage, isobaric isothermal (NPT) simulation was performed under room temperature and ambient pressure (1 bar), using velocity rescaling thermostat and Parrinello–Rahman barostat (84).

Data, Materials, and Software Availability. All study data are included in the article and/or *SI Appendix*.

ACKNOWLEDGMENTS. This work has been financially supported by the Department of Energy under the Basic Energy Sciences Award No. DE-SC0022240. NSF's ChemMatCARS, Sector 15 at the Advanced Photon Source, Argonne National Laboratory, is supported by the Divisions of Chemistry, and Materials Research, NSF, under Grant No. NSF/CHE- 1834750 and NSF/CHE-2335833. This research used resources of the Advanced Photon Source, a U.S. Department of Energy (DOE) Office of Science user facility operated for the DOE Office of Science by Argonne National Laboratory under Contract No. DE-AC02-06CH11357. The MALDI MS instrument for peptide characterization was supported by NIH S10 OD030460.

Author affiliations: [a]Department of Chemical Engineering, The City College of New York, New York, NY 10031; [b]Department of Materials Science and Engineering, Northwestern University, Evanston, IL 60208; [c]Department of Chemistry, University of Pennsylvania, Philadelphia, PA 19104; [d]Department of Chemical and Biomolecular Engineering, University of Pennsylvania, Philadelphia, PA 19104; [e]Department of Physics, University of Illinois at Chicago, Chicago, IL 60607; and [f]NSF's Chemical and Materials Science Center for Advanced Radiation Sources, School of Molecular Engineering, University of Chicago, Chicago, IL 60637

Author contributions: D.L., I.J.D., R.J.M., M.L.S., C.d.l.F.-N., R.R., E.J.P., M.O.d.l.C., R.S.T., K.J.S., and C.M. designed research; L.E.O.M., F.J.-A., J.G.M., Y.W., S.A.C., S.K.T., P.S., B.S., E.H., W.J., B.Q., W.B., M.B., and B.L. performed research; L.E.O.M., F.J.-A., J.G.M., Y.W., and W.B. analyzed data; and L.E.O.M., K.J.S., and C.M. wrote the paper.

1. J. C. G. Bünzli, C. Piguet, Taking advantage of luminescent lanthanide ions. *Chem. Soc. Rev.* **34**, 1048–1077 (2005).
2. N. C. Martinez-Gomez, H. N. Vu, E. Skovran, Lanthanide chemistry: From coordination in chemical complexes shaping our technology to coordination in enzymes shaping bacterial metabolism. *Inorg. Chem.* **55**, 10083–10089 (2016).
3. D. Parker, E. A. Suturina, I. Kuprov, N. F. Chilton, How the ligand field in lanthanide coordination complexes determines magnetic susceptibility anisotropy, paramagnetic NMR shift, and relaxation behavior. *Acc. Chem. Res.* **53**, 1520–1534 (2020).
4. K. Schulz, *Critical Mineral Resources of the United States: Economic and Environmental Geology and Prospects for Future Supply, Professional paper* (U.S. Geological Survey, 2017).
5. D. Atwood, *The Rare Earth Elements: Fundamentals and Applications* (EIC Books Wiley, 2013).
6. A. Jha, *Rare Earth Materials: Properties and Applications* (Taylor & Francis, 2014).
7. R. Tiwari, V. Dubey, V. Singh, M. Saucedo, *Luminescence: Theory and Applications of Rare Earth Activated Phosphors* (De Gruyter, 2021).
8. B. Basu, B. Banerjee, *Rare Earth Elements: Processing, Catalytic Applications and Environmental Impact* (De Gruyter, 2023).
9. N. Engineers, *Handbook on Rare Earth Metals and Alloys (Properties, Extraction, Preparation and Applications)* (NIIR Project Consultancy Services, New Delhi, India, 2009).
10. J. Lucas, P. Lucas, T. Mercier, A. Rollat, W. Davenport, *Rare Earths: Science, Technology, Production and Use* (Elsevier Science, 2014).
11. A. Golloch, *Handbook of Rare Earth Elements: Analytics, De Gruyter Reference* (De Gruyter, 2022).
12. T. Cheisson, E. J. Schelter, Rare earth elements: Mendeleev's bane, modern marvels. *Science* **363**, 489–493 (2019).
13. R. D. Shannon, Revised effective ionic radii and systematic studies of interatomic distances in halides and chalcogenides. *Acta Crystallogr., Sect. A* **32**, 751–767 (1976).
14. F. Xie, T. A. Zhang, D. Dreisinger, F. Doyle, A critical review on solvent extraction of rare earths from aqueous solutions. *Miner. Eng.* **56**, 10–28 (2014).
15. J. Florek *et al*., Selective recovery of rare earth elements using chelating ligands grafted on mesoporous surfaces. *RSC Adv.* **5**, 103782–103789 (2015).
16. N. Das, D. Das, Recovery of rare earth metals through biosorption: An overview. *J. Rare Earths* **31**, 933–943 (2013).
17. R. Braun *et al*., Peptides as biosorbents—Promising tools for resource recovery. *Res. Microbiol.* **169**, 649–658 (2018).
18. J. A. J. Cotruvo, The chemistry of lanthanides in biology: Recent discoveries, emerging principles, and technological applications. *ACS Cent. Sci.* **5**, 1496–1506 (2019).
19. J. A. Mattocks, J. A. Cotruvo, Biological, biomolecular, and bio-inspired strategies for detection, extraction, and separations of lanthanides and actinides. *Chem. Soc. Rev.* **49**, 8315–8334 (2020).
20. Q. Ye, D. Wang, N. Wei, Engineering biomaterials for the recovery of rare earth elements. *Trends Biotechnol.*, (2023).
21. T. Liu, J. Chen, Extraction and separation of heavy rare earth elements: A review. *Sep. Purif. Technol.* **276**, 119263 (2021).
22. B. T. Ngwenya *et al*., Macroscopic and spectroscopic analysis of lanthanide adsorption to bacterial cells. *Geochim. Cosmochim. Acta* **73**, 3134–3147 (2009).
23. H. Moriwaki, R. Koide, R. Yoshikawa, Y. Warabino, H. Yamamoto, Adsorption of rare earth ions onto the cell walls of wild-type and lipoteichoic acid-defective strains of *Bacillus subtilis*. *Appl. Microbiol. Biotechnol.* **97**, 3721–3728 (2013).
24. H. Moriwaki *et al*., Application of freeze-dried powders of genetically engineered microbial strains as adsorbents for rare earth metal ions. *ACS Appl. Mater. Interfaces* **8**, 26524–26531 (2016).
25. W. D. Bonificio, D. R. Clarke, Rare-earth separation using bacteria. *Environ. Sci. Technol. Lett.* **3**, 180–184 (2016).
26. P. K. R. Tay, A. Manjula-Basavanna, N. S. Joshi, Repurposing bacterial extracellular matrix for selective and differential abstraction of rare earth elements. *Green Chem.* **20**, 3512–3520 (2018).
27. H. G. Brittain, F. S. Richardson, R. B. Martin, Terbium(III) emission as a probe of calcium(II) binding sites in proteins. *J. Am. Chem. Soc.* **98**, 8255–8260 (1976).
28. B. Martin, F. S. Richardson, Lanthanides as probes for calcium in biological systems. *Q. Rev. Biophys.* **12**, 181–209 (1979).
29. L. Lee, B. D. Sykes, Use of lanthanide-induced nuclear magnetic resonance shifts for determination of protein structure in solution: EF calcium binding site of carp parvalbumin. *Biochemistry* **22**, 4366–4373 (1983).
30. S. E. Burroughs, W. D. J. Horrocks, H. Ren, C. B. Klee, Characterization of the lanthanide ion-binding properties of calcineurin-B using laser-induced luminescence spectroscopy. *Biochemistry* **33**, 10428–10436 (1994).
31. E. Pidcock, G. R. Moore, Structural characteristics of protein binding sites for calcium and lanthanide ions. *J. Biol. Inorg. Chem.* **6**, 479–489 (2001).
32. W. J. Chazin, Relating form and function of EF-hand calcium binding proteins. *Acc. Chem. Res.* **44**, 171–179 (2011).
33. M. Nitz, K. J. Franz, R. L. Maglathlin, B. Imperiali, A powerful combinatorial screen to identify high-affinity terbium(III)-binding peptides. *ChemBioChem* **4**, 272–276 (2003).
34. K. J. Franz, M. Nitz, B. Imperiali, Lanthanide-binding tags as versatile protein coexpression probes. *ChemBioChem* **4**, 265–271 (2003).
35. M. Nitz *et al*., Structural origin of the high affinity of a chemically evolved lanthanide-binding peptide. *Angew. Chem. Int. Ed. Engl.* **43**, 3682–3685 (2004).
36. L. Martin, B. Sculimbrene, M. Nitz, B. Imperiali, Rapid combinatorial screening of peptide libraries for the selection of lanthanide-binding tags (LBTs). *QSAR Comb. Sci.* **24**, 1149–1157 (2005).
37. J. A. Cotruvo, E. R. Featherston, J. A. Mattocks, J. V. Ho, T. N. Laremore, Lanmodulin: A highly selective lanthanide-binding protein from a lanthanide-utilizing bacterium. *J. Am. Chem. Soc.* **140**, 15056–15061 (2018).
38. E. C. Cook, E. R. Featherston, S. A. Showalter, J. A. Cotruvo, Structural basis for rare earth element recognition by methylobacterium extorquens lanmodulin. *Biochemistry* **58**, 120–125 (2019).
39. G. J. P. Deblonde *et al*., Selective and efficient biomacromolecular extraction of rare-earth elements using lanmodulin. *Inorg. Chem.* **59**, 11855–11867 (2020).
40. S. M. Gutenthaler *et al*., Lanmodulin peptides-unravelling the binding of the EF-hand loop sequences stripped from the structural corset. *Inorg. Chem. Front.* **9**, 4009–4021 (2022).
41. T. Hatanaka *et al*., The origins of binding specificity of a lanthanide ion binding peptide. *Sci. Rep.* **10**, 19468 (2020).
42. Z. Dong *et al*., Bridging hydrometallurgy and biochemistry: A protein-based process for recovery and separation of rare earth elements. *ACS Cent. Sci.* **7**, 1798–1808 (2021).
43. X. Xie *et al*., Broad-spectrum and effective rare earth enriching via lanmodulin-displayed *Yarrowia lipolytica*. *J. Hazard. Mater.* **438**, 129561 (2022).
44. Q. Ye, X. Jin, B. Zhu, H. Gao, N. Wei, Lanmodulin-functionalized magnetic nanoparticles as a highly selective biosorbent for recovery of rare earth elements. *Environ. Sci. Technol.* **57**, 4276–4285 (2023).
45. D. M. Park *et al*., Bioadsorption of rare earth elements through cell surface display of lanthanide binding tags. *Environ. Sci. Technol.* **50**, 2735–2742 (2016).
46. D. M. Park, A. Brewer, D. W. Reed, L. N. Lammers, Y. Jiao, Recovery of rare earth elements from low-grade feedstock leachates using engineered bacteria. *Environ. Sci. Technol.* **51**, 13471–13480 (2017).
47. D. Park *et al*., A biosorption-based approach for selective extraction of rare earth elements from coal byproducts. *Sep. Purif. Technol.* **241**, 116726 (2020).
48. E. Chang, A. W. Brewer, D. M. Park, Y. Jiao, L. N. Lammers, Surface complexation model of rare earth element adsorption onto bacterial surfaces with lanthanide binding tags. *Appl. Geochem.* **112**, 104478 (2020).
49. X. Xie *et al*., Effectively auto-regulated adsorption and recovery of rare earth elements via an engineered *E. coli*. *J. Hazard. Mater.* **424**, 127642 (2022).
50. G. Verma *et al*., Investigation of rare earth element binding to a surface-bound affinity peptide derived from EF-hand loop I of lanmodulin. *ACS Appl. Mater. Interfaces* **16**, 16912–16926 (2024).
51. J. D. Hostert, M. R. Sepesy, C. E. Duval, J. N. Renner, Clickable polymer scaffolds enable Ce recovery with peptide ligands. *Soft Matter* **19**, 2823–2831 (2023).
52. Z. Hussain *et al*., Repeated recovery of rare earth elements using a highly selective and thermo-responsive genetically encoded polypeptide. *Adv. Funct. Mater.* **32**, 2109158 (2022).
53. R. Lemlich, *Adsorptive Bubble Separation Techniques* (Elsevier Science, 2012).

54. G. Gallios, K. Matis, *Mineral Processing and the Environment, NATO Science Partnership Subseries: 2* (Springer, Netherlands, 2010).
55. W. Peng *et al*., An overview on the surfactants used in ion flotation. *J. Mol. Liq.* **286**, 110955 (2019).
56. C. Micheau, O. Diat, P. Bauduin, Ion foam flotation of neodymium: From speciation to extraction. *J. Mol. Liq.* **253**, 217–227 (2018).
57. C. Micheau, A. Schneider, L. Girard, P. Bauduin, Evaluation of ion separation coefficients by foam flotation using a carboxylate surfactant. *Colloids Surf., A* **470**, 52–59 (2015).
58. S. Shetty IV, S Ponnurangam Chernyshova, Foam flotation of rare earth elements by conventional and green surfactants. *Miner. Eng.* **158**, 106585 (2020).
59. M. Miller *et al*., Electrostatic origin of element selectivity during rare earth adsorption. *Phys. Rev. Lett.* **122**, 058001 (2019).
60. J. R. Haas, E. L. Shock, D. C. Sassani, Rare earth elements in hydrothermal systems: Estimates of standard partial molal thermodynamic properties of aqueous complexes of the rare earth elements at high pressures and temperatures. *Geochim. Cosmochim. Acta* **59**, 4329–4350 (1995).
61. C. Baes, R. E. Mesmer, *The Hydrolysis of Cations 1976* (RE Krieger, Malabar, FL, 1986).
62. P. L. Brown, C. Ekberg, *Hydrolysis of Metal Ions* (John Wiley & Sons, 2016).
63. D. Graham, M. Phillips, Proteins at liquid interfaces: I. Kinetics of adsorption and surface denaturation. *J. Colloid Interface Sci.* **70**, 403–414 (1979).
64. D. Graham, M. Phillips, Proteins at liquid interfaces: II. Adsorption isotherms. *J. Colloid Interface Sci.* **70**, 415–426 (1979).
65. D. Graham, M. Phillips, Proteins at liquid interfaces: III. Molecular structures of adsorbed films. *J. Colloid Interface Sci.* **70**, 427–439 (1979).
66. D. Graham, M. Phillips, Proteins at liquid interfaces. IV. Dilatational properties. *J. Colloid Interface Sci.* **76**, 227–239 (1980).
67. D. Graham, M. Phillips, Proteins at liquid interfaces. V. Shear properties. *J. Colloid Interface Sci.* **76**, 240–250 (1980).
68. J. R. Hunter, P. K. Kilpatrick, R. G. Carbonell, Lysozyme adsorption at the air/water interface. *J. Colloid Interface Sci.* **137**, 462–482 (1990).
69. R. Miller *et al*., Experimental studies on the desorption of adsorbed proteins from liquid interfaces. *Food Hydrocolloids* **19**, 479–483 (2005).
70. B. C. Tripp, J. J. Magda, J. D. Andrade, Adsorption of globular proteins at the air/water interface as measured via dynamic surface tension: Concentration dependence, mass-transfer considerations, and adsorption kinetics. *J. Colloid Interface Sci.* **173**, 16–27 (1995).
71. R. Douillard, J. Lefebvre, V. Tran, Applicability of Gibbs' law to protein adsorption isotherms. *Colloids Surf., A* **78**, 109–113 (1993).
72. D. Vaknin, W. Bu, Neutrally charged gas/liquid interface by a catanionic Langmuir monolayer. *J. Phys. Chem. Lett.* **1**, 1936–1940 (2010).
73. P. Pershan, M. Schlossman, *Liquid Surfaces and Interfaces: Synchrotron X-Ray Methods* (Cambridge University Press, 2012).
74. M. Bera, W. Bu, Xmodfit Version 1.0.0 (2022). https://github.com/chemmatcars/XModFit. Accessed 1 May 2024.
75. W. Bu *et al*., X-ray studies of interfacial strontium-extractant complexes in a model solvent extraction system. *J. Phys. Chem. B* **118**, 12486–12500 (2014).
76. W. Bu *et al*., Observation of a rare earth ion-extractant complex arrested at the oil–water interface during solvent extraction. *J. Phys. Chem. B* **118**, 10662–10674 (2014).
77. S. Pall *et al*., Heterogeneous parallelization and acceleration of molecular dynamics simulations in GROMACS. *J. Chem. Phys.* **153**, 134110 (2020).
78. B. Hess, C. Kutzner, D. van der Spoel, E. Lindahl, GROMACS 4: Algorithms for highly efficient, load-balanced, and scalable molecular simulation. *J. Chem. Theory Comput.* **4**, 435–447 (2008).
79. R. B. Best *et al*., Optimization of the additive CHARMM all-atom protein force field targeting improved sampling of the backbone φ, ψ and side-chain χ^1 and χ^2 dihedral angles. *J. Chem. Theory Comput.* **8**, 3257–3273 (2012).
80. B. Qiao, S. Skanthakumar, L. Soderholm, Comparative CHARMM and amoeba simulations of lanthanide hydration energetics and experimental aqueous-solution structures. *J. Chem. Theory Comput.* **14**, 1781–1790 (2018).
81. U. Essmann *et al*., A smooth particle mesh Ewald method. *J. Chem. Phys.* **103**, 8577–8593 (1995).
82. H. C. Andersen, Rattle: A "velocity" version of the shake algorithm for molecular dynamics calculations. *J. Comput. Phys.* **52**, 24–34 (1983).
83. G. Bussi, D. Donadio, M. Parrinello, Canonical sampling through velocity rescaling. *J. Chem. Phys.* **126**, 014101 (2007).
84. M. Parrinello, A. Rahman, Polymorphic transitions in single crystals: A new molecular dynamics method. *J. Appl. Phys.* **52**, 7182–7190 (1981).